ELSEVIER

Contents lists available at ScienceDirect

# Colloids and Surfaces A: Physicochemical and Engineering Aspects

journal homepage: www.elsevier.com/locate/colsurfa



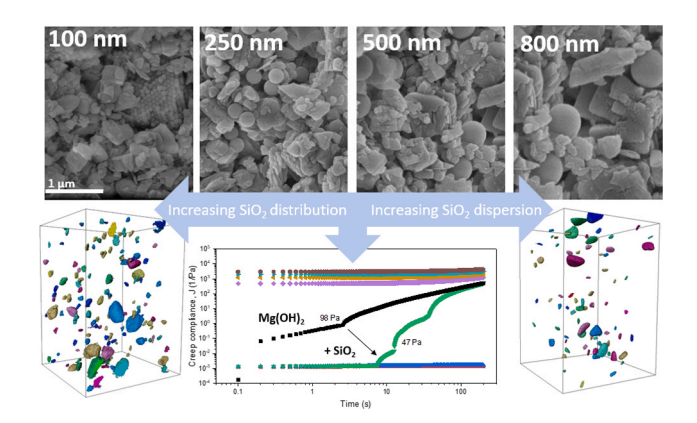


# Yielding mechanisms in binary suspensions of colloidal Mg(OH)<sub>2</sub> and spherical SiO<sub>2</sub> particles

Olivia Pickup <sup>a</sup>, Leonard Turpin <sup>b</sup>, Vyacheslav Kachkanov <sup>b</sup>, Alexander Lockwood <sup>c</sup>, Martyn Barnes <sup>c</sup>, Timothy Hunter <sup>a</sup>, David Harbottle <sup>a,\*</sup>

- <sup>a</sup> School of Chemical and Process Engineering, University of Leeds, Leeds LS2 9JT, UK
- <sup>b</sup> Diamond Light Source Ltd, Harwell Science and Innovation Campus, Didcot OX11 ODE, United Kingdom
- <sup>c</sup> Sellafield Ltd, Hinton House, Birchwood Park Ave, Birchwood, Warrington WA3 6GR, UK

#### GRAPHICAL ABSTRACT



# ARTICLE INFO

Keywords: Yield stress Nanoparticle lubrication Nanoparticle dispersion Large amplitude oscillatory shear Creep rheology

# ABSTRACT

The yield stress of magnesium hydroxide  $(Mg(OH)_2)$  suspensions can be significantly reduced by adding a low vol % of spherical nano silica to the suspension. The nano silica acts to lubricate the contacts between the irregularly shaped  $Mg(OH)_2$  by interrupting the aggregated structure and acting akin to a ball-bearing, which allows particles to rotate past one another with little resistance. The dependence on nanoparticle size (100, 250, 500 and 800 nm) and concentration (blending ratios  $Mg(OH)_2:SiO_2 - 27:3$ , 28:2, 29:1 (vol%:vol%)) was found to be directly influenced by the dispersion (number of dispersed particles) and distribution of particles throughout the  $Mg(OH)_2$  network. Creep rheology identified a multi-step yielding process to transition from an abrupt, brittle yield in  $Mg(OH)_2$  suspensions to a more gradual, softer yield with  $SiO_2$ . Large amplitude oscillatory shear (LAOS) revealed variations in intracycle strain stiffening and energy dissipation, with  $500 \text{ nm } SiO_2$  promoting the most effective disruption of the  $Mg(OH)_2$  network. Microstructural analysis via SEM and X-ray computed tomography confirmed that  $500 \text{ nm } SiO_2$  achieved optimal dispersion and distribution due to minimal clustering. These results highlight the critical relationship between nanoparticle size, dispersion, and number ratio between large

E-mail address: d.harbottle@leeds.ac.uk (D. Harbottle).

 $<sup>^{\</sup>star}$  Corresponding author.

and small particles in tuning the rheology of concentrated suspensions, offering new insights for the mechanisms of yield stress modification in binary particle systems.

#### 1. Introduction

Suspensions of cohesive or aggregated particles can exhibit complex yielding behavior[1–3]. The yield stress, defined as the minimum applied stress required to overcome the strength of the particulate network and initiate flow, depends on various factors, including solids volume fraction, particle shape, size, surface roughness, and the strength of interparticle interactions. Controlling yield stress is critical in a wide range of applications, from processing nuclear waste sludge to designing the texture of food products[4–6]. Common strategies for modifying yield stress include the addition of polymeric dispersants, adjustments to the solution chemistry – pH and electrolyte concentration[7–9], and the introduction of depletion interactions via non-adsorbing species[10]. Additionally, the flow behavior of dense colloidal suspensions can be altered by incorporating small nanoparticles into the matrix of larger, fractal aggregates[11], although the underlying mechanism(s) governing this modification remain to be debated.

In binary suspensions of colloidal particles, interactions between the two particle types play a crucial role in determining the stability and structure of the suspension. For oppositely charged colloids, electrostatic attraction can lead to heteroaggregation, with the resulting structures influenced by factors such as charge density, particle size ratio, and mixing ratio[12]. As charge-neutral aggregates form, the colloidal stability decreases, leading to sedimentation or the development of network structures with viscoelastic properties[13].

Particle size plays a pivotal role in governing many of these effects. Yates et al. systematically demonstrated that the optimal number of smaller silica nanoparticles required to induce aggregation of larger alumina particles decreased markedly as the particle size ratio (silica/ alumina) increased[14]. When the size ratio approached unity, aggregation could be achieved with a near one-to-one particle number ratio, indicating high aggregation efficiency. In contrast, at very low size ratios (<0.025), the number of small particles required for aggregation far exceeded the theoretical estimate for half surface coverage (considered optimum for aggregation), implying there is a significant fraction of non-contributing particles. The authors attributed this to the adsorption of smaller particles within the interstitial spaces between larger particles, as well as to factors such as surface roughness and deviations from perfect sphericity, which likely become more important as silica particle size decreases. While the dispersion of silica may also have influenced behavior, this was not discussed by the authors.

More recently, Cerbelaud et al. demonstrated that the adsorption of silica nanoparticles onto large alumina platelets promoted deagglomeration rather than agglomeration, leading to denser and more ordered sediment structures being formed[15]. This behavior was attributed to the progressive surface coating of alumina by negatively charged silica nanoparticles, which reversed the surface potential and increased electrostatic repulsion between the alumina platelets. The authors proposed that the enhanced repulsive forces improved particle mobility and facilitated the alignment of platelets during sedimentation. However, the study assumed complete interaction between silica and alumina, without considering the potential influence of free or unbound silica nanoparticles in the suspension, which is likely to contribute to particle mobility during sediment bed consolidation.

Rheological modification of binary suspensions has been demonstrated in clay-based systems, with effects ranging from gel strengthening to complete liquefaction, depending on the system composition and interaction mechanisms[16–18]. Research has investigated how silica nanoparticles, mostly Ludox, modulate the viscoelastic behaviour of smectite clays. The mechanisms underlying these rheological changes are often attributed to a combination of electrostatic interactions,

structural disruption, and depletion forces, though these mechanisms are rarely evidenced. Kleshchanok et al. hypothesised that spherical colloids adsorb onto the edges of clay particles, preventing the formation of the "house-of-cards" structure in weak gels and thereby promoting liquefaction[16]. In contrast, for stronger gels, the colloids were proposed to adsorb less on the edges and more on the basal planes, increasing the spacing between clay particles to weaken interparticle interactions.

Rheological enhancement tends to be better understood, particularly in systems involving oppositely charged particles. These form heteroflocculated gel networks, where network strength correlates with the concentration of added particles and their efficiency in coating the primary particles, similar to the mechanisms previously described to destabilize colloidal suspensions. Many of the mechanisms to modify rheology in dilute suspensions are reviewed by Bailey et al., who discussed the different scenarios involving oppositely and similarly charged binary components, as well as the influence of particle shape [19].

The rheology of concentrated particle suspensions can also be modified by the addition of spherical nanoparticles, with one key mechanism being nanoparticle haloing[20]. In this process, small, highly charged nanoparticles form a diffuse shell, or "halo", around larger primary particles, enhancing interparticle repulsion, stabilising the suspension, and reducing its viscosity. The authors showed there is an optimal blend ratio for achieving maximum viscosity reduction. When too few silica nanoparticles are present, complete monolayer halos cannot form around alumina particles, limiting the effect. At the optimal ratio, the suspension exhibits an almost Newtonian-like response, enabled by both sufficient silica concentration to form complete halos and a bulk fluid containing enough well-stabilised silica sol nanoparticles. However, at higher silica loadings, viscosity increases again due to the rising overall solids volume fraction, which diminishes the effectiveness of the haloing mechanism.

Recent simulations by Singh et al. likely provide insight in the behavior induced by the excess silica in the bulk fluid[21]. Studying dense, bidisperse, non-Brownian suspensions, their findings reveal that the inclusion of small, non-adsorbing particles can lower viscosity and shift the jamming threshold to higher solids fractions. This effect was attributed to a redistribution of stress-bearing contacts: as the concentration of small particles increases, the dominant stress pathways shift from large-large to small-small contacts. This microstructural reorganisation fundamentally alters the flow behaviour, allowing suspensions to remain fluid at higher packing densities. This effect has also been discussed by Chaki et al., who observed that elastic energy storage in dense particulate networks shifts from being governed by the colloidal particles at low nanoparticle packing fractions, to the nanoparticles themselves at high nanoparticle concentrations[22]. The authors further extended their study to investigate the effect of particle size ratio, showing that larger size ratios were more effective at reducing the elastic shear modulus relative to the hard-sphere model, contrasting the more comparable size ratios that enhanced the shear modulus. It is worth noting that these effects were observed at colloidal packing fractions below 56 vol%, with the elastic shear modulus showing only a weak dependence on size ratio at higher concentrations.

While there is a growing understanding of the mechanisms that govern rheological modification in binary particle suspensions, and the role of colloidal interactions in controlling such behaviour is well established, our recent work has demonstrated that yield stress reduction can occur in concentrated suspensions of two weakly attractive particles at nanoparticle concentrations significantly lower than those reported[11]. To investigate this behavior further, the present study

examines how particle size ratio influences yield stress reduction, specifically assessing whether the effect remains as the size ratio approaches unity. Yield stress behavior and the underlying yielding mechanisms are characterised using creep tests and large amplitude oscillatory shear (LAOS) measurements.

#### 2. Materials and methods

Magnesium hydroxide (Mg(OH)) $_2$  (Versamag, Martin Marietta, US) with a density of 2.26 g/cm $^3$  and colloidal silica (AngstromSphere, Fiber Optic Center, US) with a density of 1.88 g/cm $^3$  were used as received. The particle size of Mg(OH) $_2$  was measured by dynamic light scattering (Mastersizer 3000, Malvern Panalytical, UK) to determine the aggregate size in the background electrolyte, and a BET surface area analyzer (Micrometrics TriStar 3000, Malvern Panalytical) was used measure the approximate (assumed spherical[23]) primary particle size as dprimary (nm) =  $\frac{6000}{SSA\bullet p}$ , where SSA is the measured specific surface area (m $^2$ /g) and  $\rho$  the particle density (g/cm $^3$ ). The Zetasizer Advance (Malvern Panalytical, UK) was used to measure the d $_{50}$  of the SiO $_2$  particles which had a manufacture quoted particle size of 100, 250, 500 and 800 nm. The particle size distributions of the Mg(OH) $_2$  and SiO $_2$  are shown in the Supporting Information, Fig. S1.

The suspensions were prepared by slowly adding Mg(OH)<sub>2</sub> powder to  $10^{-3}$  M NaCl at the natural buffered pH of 9.6 and stirred using a low-shear overhead mixer (DLAB, SciQuip) at 600 rpm for 10 min, before being left to gently agitate overnight on an orbital shaker (Stuart SSL1). The SiO<sub>2</sub> particles were also prepared in  $10^{-3}$  M NaCl, shaken manually and sonicated for 10 min before being gently agitated overnight. After 24 h, the SiO<sub>2</sub> suspension was tip sonicated for 10 min (ultrasonic probe, Fisher Scientific) and then added dropwise to the Mg(OH)<sub>2</sub> suspension while stirring at 800 rpm. The blended suspensions were left to mix for a further 24 h before use.

**Imaging techniques:** Scanning electron microscope (SEM) images of the binary suspensions were taken using a Hitachi SU8230 SEM. A voltage of 5 kV was used with a current of 15600 nA and magnification range between  $10,000\times-30,000\times$ .

Synchrotron X-ray computed tomography at Diamond Light Source: Utilizing beamline I13-2, a pink beam with a centre energy of approximately 27 keV was filtered through a 140 µm Fe filter and a 20 µm Ni foil to prevent the sample from boiling. Projections were recorded using a PCO Edge 5.5 camera at 4 × magnification, yielding a pixel size of  $1.625 \, \mu m$  and a field of view of  $4.2 \times 3.5 \, mm$ . Binary suspensions were prepared following outlined procedures, and 1.5 mL was subsampled and sealed in a polypropylene tube (Eppendorf Tubes® 3810X) for mounting on the tomography stage. Each projection had an exposure time of 0.2 s, with a total acquisition time of 13 min. Tomographic reconstructions were carried out using the Savu 3.0 processing pipeline prior to generating the 3D volume[24]. Image post-processing was performed using Avizo 2022.1 Software (ThermoFisher Scientific, UK). A sub-volume of the full scan volume (2066  $\times$  2323  $\times$  3413  $\mu m^3$ ) was extracted, and a series of image filters were applied before threshold segmentation of SiO<sub>2</sub> to isolate cluster volumes  $\geq 1 \times 10^5 \, \mu \text{m}^3$  for volume analysis.

**Rheology:** A DHR-2 rheometer (TA Instruments, UK) was used for rheological measurements. A four bladed vane geometry (Peltier Steel 109325, diameter = 15 mm, length = 38 mm) and sand blasted cup (diameter = 29.2 mm) were used for oscillatory studies, and a larger vane (Peltier Steel 108623, diameter = 28 mm, length = 42 mm) was used for creep measurements to minimise any wall effects [25]. The instrument was calibrated before each use, and a sample volume of 40 mL was transferred into the cup before lowering the upper geometry to the operating gap (8800  $\mu$ m) and a solvent trap was used to prevent sample drying. Before each test a standard pre-shear protocol was used to eliminate any sample transfer effects, this involved applying shear at 300 s<sup>-1</sup> for 60 s before leaving the sample to equilibrate in the sample

cup for 60 s with no shear. The yield stress was measured using a creep procedure applying a constant stress hold below the rotationally measured yield stress for 200 s before a recovery of 200 s. After each recovery step the constant stress was increased by a multiplication factor of 1.05. The yield stress range was taken from the stress limit prior to yield and the stress during which the sample creep compliance increased. LAOS strain amplitude sweep experiments were conducted from  $1\times10^{-4}-1000$ % strain at 10 rad/s. The data was collected in transient mode, using conditioning and sampling times of 3 s, and collecting 153 points per cycle. Newly prepared suspensions were used for repeat measurements. Frequency sweep experiments were performed between 0.05-100 rad/s at a constant strain value (3  $\times$  10 $^{-3}\%$ ) within the LVR determined from the amplitude sweep.

#### 3. Results and discussion

SiO<sub>2</sub> dispersion and distribution: SEM images of suspensions with the same Mg(OH)<sub>2</sub> volume fraction (28 vol%) and SiO<sub>2</sub> volume fraction (2 vol%) but with different SiO<sub>2</sub> particle sizes are shown in Fig. 1. The Mg(OH)<sub>2</sub> particles are irregularly shaped and mostly plate-like, with a primary particle size of 250 nm determined by BET and an aggregate size of 5 µm measured by dynamic light scattering (DLS)[11]. In contrast, the colloidal silica particles are smooth and spherical, and distributed throughout the Mg(OH)<sub>2</sub> network, with the d<sub>50</sub> particle size measured by DLS to be 102 nm (100 nm sample), 255 nm (250 nm sample), 513 nm (500 nm sample) and 720 nm (800 nm sample). The manufacturing quoted sizes are used throughout the discussion for simplicity. The SEM images show the larger silica particles to be better dispersed, with the smaller 100 nm SiO<sub>2</sub> forming small aggregates and large clusters that consume hundreds of particles. The clustering of the smaller silica is due to the increased cohesion forces in the dry powder, with the electrostatic cohesion between particles increasing for a higher surface area to volume ratio per particle mass[26]. Even though the SiO<sub>2</sub> suspension is tip sonicated prior to blending with the Mg(OH)2 suspension, it seems the energy is insufficient to entirely disperse the smaller SiO<sub>2</sub> particles.

Also shown in Fig. 1 and previously discussed [11], the 100 nm  $\rm SiO_2$  particles do not coat the larger Mg(OH)<sub>2</sub> particles, even though there is a sufficient number of particles to do so. This likely results from only a weak colloidal attraction between the two particles types, with the zeta potentials of Mg(OH)<sub>2</sub> and  $\rm SiO_2$  particles being + 5 mV and - 30 mV, respectively. It is also worth noting that for the larger  $\rm SiO_2$  particles, less particles were observed within the same imaged area, due to the lower particle number ratio when the two particle types are equivalent in size.

Using X-ray computed tomography, the SiO<sub>2</sub> clusters and their distribution throughout the Mg(OH)<sub>2</sub> network (binary suspensions of Mg (OH)<sub>2</sub>:SiO<sub>2</sub> at 28:2 vol%:vol%) were visualized based on the contrasting X-ray attenuation of the two materials (Fig. 2). Due to the instrument resolution limits, only SiO<sub>2</sub> clusters  $> 1\times 10^5~\mu\text{m}^3$  were measured, giving an indication of the larger cluster sizes present rather than identifying all individual particles. The volume histogram data agrees with the SEM observations (Fig. 1), with fewer large clusters seen for the larger SiO<sub>2</sub> particles, confirming better dispersion of these particles. The total number of counted clusters was 155 for 100 nm SiO<sub>2</sub>, 143 for 250 nm SiO<sub>2</sub>, 36 for 500 nm SiO<sub>2</sub> and 79 for 800 nm SiO<sub>2</sub>.

The approximate number ratios for  $Mg(OH)_2$  to  $SiO_2$  based on both the  $d_{primary}$  and  $d_{50}$  of  $Mg(OH)_2$  are summarized in Table 1. It should be noted that those ratios represent the probable upper and lower bounds, with the true ratio expected to lie between them. From image analysis, the total cluster volume in each sample was used to approximate the percentage of  $SiO_2$  particles below the threshold volume, relative to the amount of  $SiO_2$  added. The dispersed fraction of  $SiO_2$  particles below the threshold cluster size was 59 %, 80 %, 97 % and 83 % for the 100, 250, 500 and 800 nm  $SiO_2$  particles respectively (Table 1), confirming very high dispersibility of the 500 nm particles. Taking those values, the  $d_{50}$  number ratio can be adjusted for the large  $SiO_2$  clusters, with the

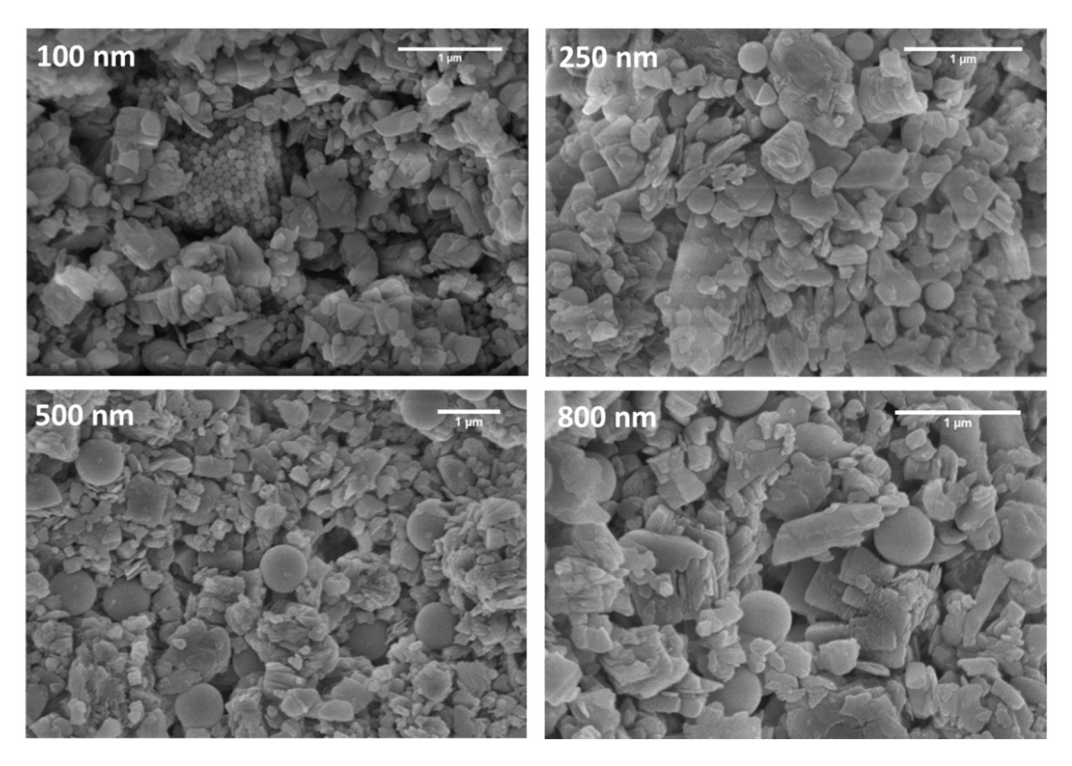


Fig. 1. Scanning electron microscopy images of the binary suspensions of  $Mg(OH)_2$  and  $SiO_2$  prepared at 28:2 vol%:vol% using 100, 250, 500 and 800 nm  $SiO_2$  particles.

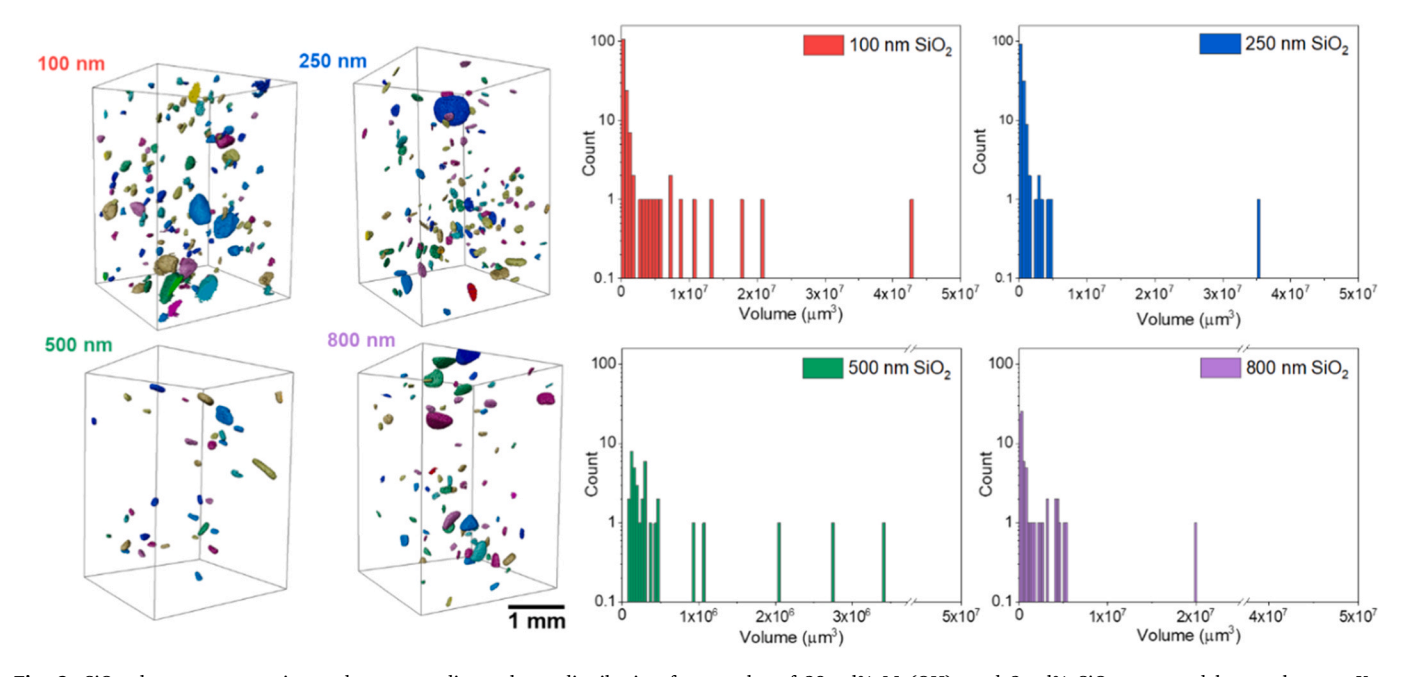


Fig. 2.  $SiO_2$  cluster segmentation and corresponding volume distribution for samples of 28 vol% Mg(OH)<sub>2</sub> and 2 vol%  $SiO_2$  measured by synchrotron X-ray computed tomography. Minimum cluster size volume for analysis  $> 1 \times 10^5 \, \mu m_{\odot}^3$  Total counts: 155 for 100 nm  $SiO_2$ , 143 for 250 nm  $SiO_2$ , 36 for 500 nm  $SiO_2$  and 79 for 800 nm  $SiO_2$ .

corrected ratios for 100, 250, 500 and 800 nm  $\rm SiO_2$  particles being 1:4960, 1:430, 1:64 and 1:20, respectively. Even after adjustment, the 100 and 250 nm  $\rm SiO_2$  particles remain in great excess of the Mg(OH)<sub>2</sub> particles.

**Binary suspension yielding:** Fig. 3 compares the creep rheology of the Mg(OH) $_2$  suspension and Mg(OH) $_2$  + SiO $_2$  binary suspensions. When adding 2 vol% SiO $_2$  to 28 vol% Mg(OH) $_2$  the yield stress reduced from 93 – 98 Pa without any silica (Fig. 3a) to 63 – 66 Pa with 100 nm silica

(Fig. 3b). Further reductions were seen to 55-47 Pa and 45-47 Pa when adding 250 nm (Fig. 3c) and 500 nm (Fig. 3d) silica, respectively. Adding 800 nm silica led to a reduced yield stress similar to that of the 100 nm particles, 60-63 Pa (Fig. 3e), even though the number ratios of the two binary suspensions are significantly different (Table 1). A reduced yield stress when adding the larger 800 nm  $SiO_2$  particles further supports our concept that the spherical  $SiO_2$  acts like a ball bearing to modify the contact mechanics between the irregularly shaped

Table 1 Variation in the approximate Mg(OH)<sub>2</sub>:SiO<sub>2</sub> number ratio (assuming complete dispersion) and the corresponding percentage of dispersed SiO<sub>2</sub>.

|  |                                 | 100 nm | 250 nm | 500 nm  | 800 nm  |
|--|---------------------------------|--------|--------|---------|---------|
| Number ratio of Mg<br>(OH) <sub>2</sub> :SiO <sub>2</sub> in | 250 nm<br>d <sub>primary</sub>  | 1:2    | 1:0.07 | 1:0.008 | 1:0.003 |
| 28:2 vol%:vol%   | 5 μm<br>cluster d <sub>50</sub> | 1:8400 | 1:540  | 1:66    | 1:24    |
| Percentage of SiO <sub>2</sub> dispersed in scanned volume   |                                 | 59 %   | 80 %   | 97 %    | 83 %    |

 ${\rm Mg(OH)_2}$  particles. Other mechanisms which have been proposed such as coating of larger particles by smaller particles that have different isoelectric points [15,27], thus changing the electric double layer interaction between the particles, and the formation of small particle networks that shifts the stress distribution from large particle contacts to small particle contacts[21], are not valid mechanisms based on the images previously shown.

As well as lowering the yield stress, the mechanism of yielding appears different based on interpreting the three distinct regions of creep yielding: i) primary creep (elastic creep resistance), ii) secondary creep (time dependent viscoelastic deformation), and iii) tertiary creep (viscous flow) (Fig. 3). Without SiO<sub>2</sub>, the Mg(OH)<sub>2</sub> network undergoes

instantaneous vielding, with no measurable primary creep before yielding, only secondary creep (ii), and then tertiary creep for any stress applied above the yield stress (iii). For suspensions with 100, 250 and 500 nm SiO<sub>2</sub>, and at the critical applied stress, all three regions are observed, beginning with prolonged elastic creep resistance measured over several seconds (i), followed by time dependent viscoelastic deformation that showed varying rates of creep compliance. The transition during region (ii) shows multiple reductions in the creep compliance rate, indicative of a multi-step yielding process, which is more prominent in samples with the lowest yield stresses (C - 250 nm and D - 500 nm). These steps within the yielding transition suggest the system becomes more ductile with the addition of SiO<sub>2</sub>, before complete steady-state viscous flow occurs at the higher stresses (iii). The sample with 800 nm SiO<sub>2</sub> appears similar to that without SiO<sub>2</sub>, showing almost no elastic creep resistance prior to time dependent viscoelastic deformation, which is likely due to the minimal amount of SiO<sub>2</sub> present to sufficiently induce more gradual, stepwise yield.

The frequency dependent viscoelastic properties of the suspensions were compared at a constant strain of  $3\times10^{-3}$  % (within the LVR) and for an increasing angular frequency from 0.01 to 100 rad/s (Fig. 4a). The G' and G" responses show a weak frequency dependence which is indicative of a soft glassy rheology (SGR) material. The SGR model describes the behavior of strongly aggregated materials that exhibit

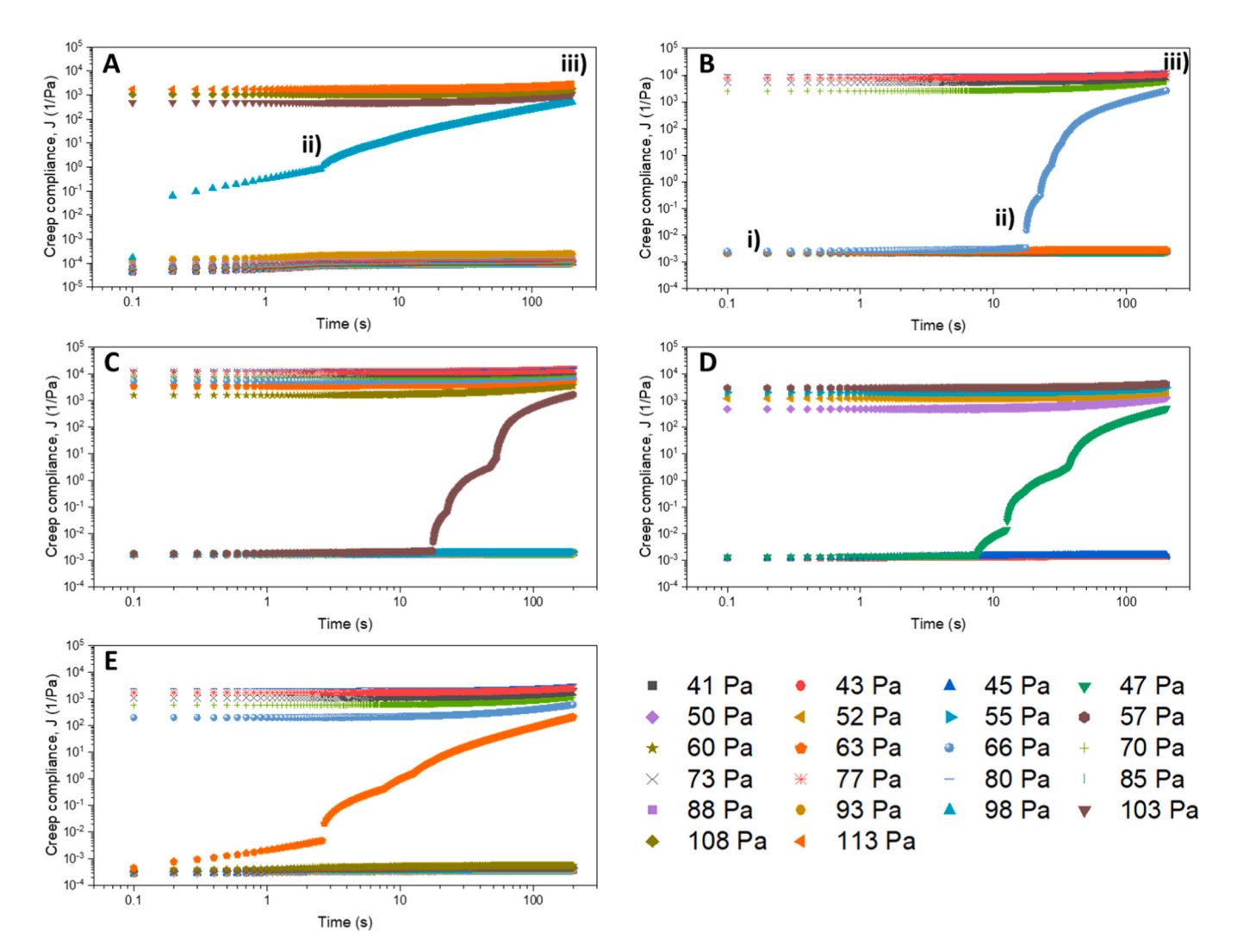


Fig. 3. Creep compliance of  $Mg(OH)_2$  and  $Mg(OH)_2$ :  $SiO_2$  binary suspensions. A) 28 vol%  $Mg(OH)_2$  only and with 2 vol% added at B) 100 nm, C) 250 nm, D) 500 nm and E) 800 nm  $SiO_2$ . Measured with 200 s applied stress and 200 s recovery. Yield stress region indicated by increased compliance on Y-axis, noted as 3 regions, i) elastic creep resistance prior to yield, ii) time dependent deformation and iii) tertiary creep (viscous flow).

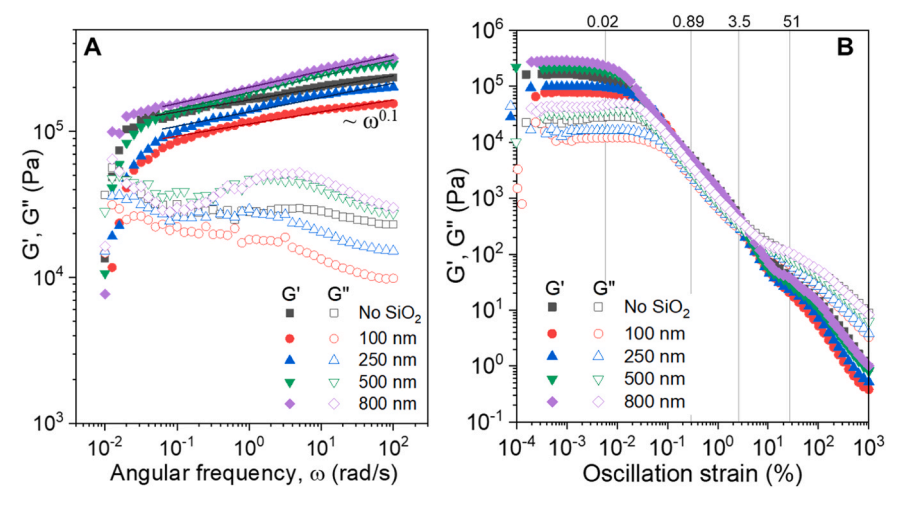


Fig. 4. A) Frequency sweep from 0.01-100 rad/s at  $3\times10^{-3}$  % strain. Straight lines show the soft glassy rheology power law fitting, with G' exponents of  $\sim0.1$  for all samples. B) Strain amplitude sweep for 28:2 vol%:vol% Mg(OH)<sub>2</sub>:SiO<sub>2</sub> indicating 4 different points during the yield, 0.02 % (end of LVR), 0.89 % (during yield), 3.5 % (G'<sub>1</sub>/G"<sub>1</sub> crossover) and 51 % (plastic flow).

metastable structures. These materials are characterised by a yield stress, pronounced viscoelasticity, and ageing, arising from their jammed microstructures where particles are trapped in energy wells (cages) formed by their neighbours. Under shear within the LVR, these structures can undergo local rearrangements, referred to as "cage breaking", allowing the particles to escape their confinement and transition to lower energy configurations[28]. Each structural element is considered to be trapped in an energy well of depth  $x_g$ , and the likelihood of escape from these wells depends on the effective noise temperature x, which reflects the intensity of mechanical fluctuations or internal noise within the system[29–31]. The G' modulus exhibits a power-law dependence on frequency, with the complex modulus  $G(\omega)$  scaling as  $\omega^{\delta}$ , where the

exponent  $\delta=x-1$ , assuming a characteristic energy barrier depth  $x_g=1$ . A material is in the soft glassy regime when the effective noise temperature x lies between 1 and 2. At x=1, the system exhibits a finite yield stress, indicative of arrested dynamics, while for x>2, the material approaches Maxwellian (fluid-like) behavior with exponential stress relaxation. Fig. 4a shows the SGR model fitting for all samples, with a measured exponent  $\delta\approx0.1$  corresponding to x>1. This confirms that the suspensions are within the soft glassy regime, characterized by slow dynamics and weakly yielding behavior.

Strain amplitude sweeps (0.001–1000 % strain at 10 rad/s) revealed similar yielding behavior for all samples (Fig. 4b). Within the LVR, all samples exhibited elastic solid-like behavior characterized by G' > G'',

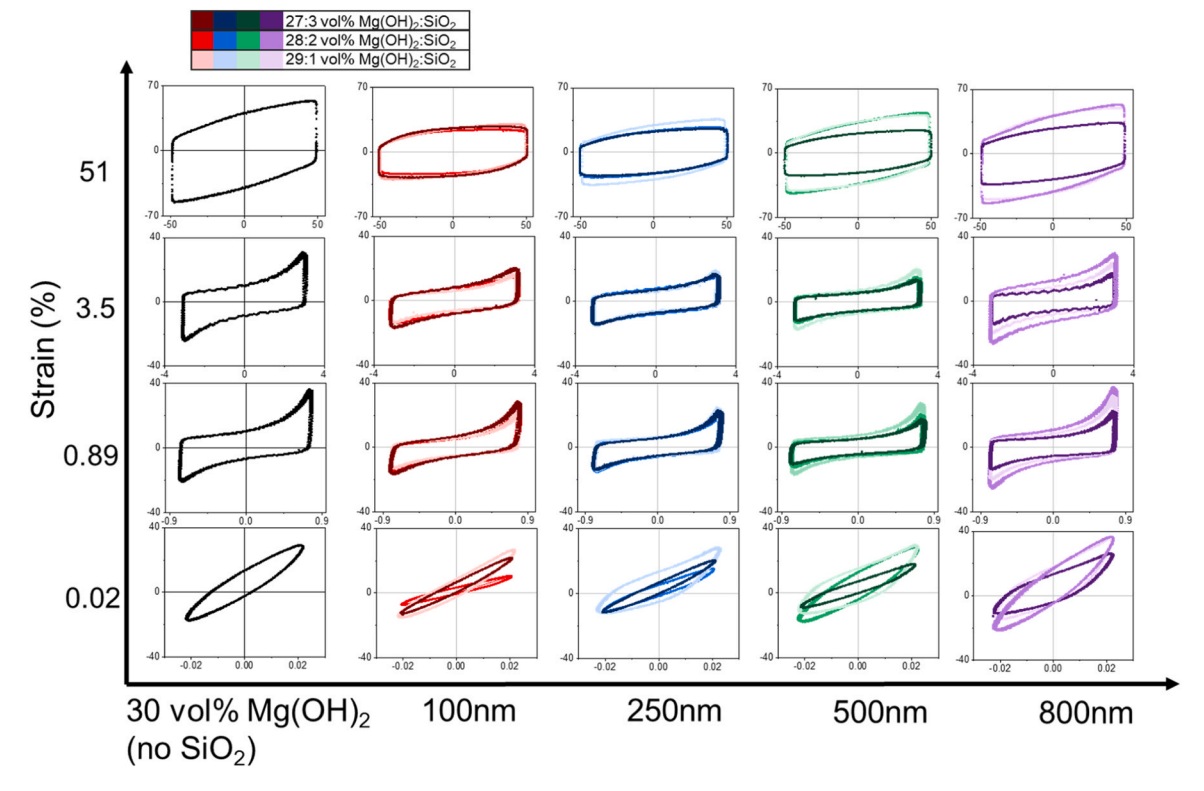


Fig. 5. Lissajous plots for suspensions of  $Mg(OH)_2$  (black) and binary suspensions containing  $Mg(OH)_2$  and  $SiO_2 - 100$  nm = red, 250 nm = blue, 500 nm = green, 800 nm = purple). Lissajous Y and X axes represent the intracycle stress vs strain respectively. Binary  $Mg(OH)_2$ :SiO<sub>2</sub> concentrations studied were 29:1 vol%:vol% (light shade), 28:2 vol%:vol% (medium shade) and 27:3 vol%:vol% (dark shade).

followed by a crossover of the apparent moduli  $G^{"}_{1} > G^{'}_{1}$  at  $\sim \! \! 3.5 \, \%$  strain. While the overall yielding behavior appeared similar in the amplitude sweep data, subtle differences in the yielding mechanics are not readily discernible, thus it is important to analyse the intracycle strain against stress behaviour at different strain amplitudes – prior to, during and after yielding.

At each applied strain amplitude, the corresponding deformation response was measured and visualized using Lissajous curves, which represent the intracycle relationship between stress and strain during large amplitude oscillatory shear (LAOS) experiments[18,19]. These plots were generated at four representative strain amplitudes to capture distinct mechanical regimes: (i) 0.02 % - within the LVR, (ii) 0.89 % near the onset of nonlinearity, (iii) 3.5 % – at the crossover point of the G'<sub>1</sub> and G''<sub>1</sub> moduli, and (iv) 51 % – in the regime of plastic flow (Fig. 5). Each Lissajous curve is displayed on axes of applied strain versus resulting stress. At  $\gamma = 0.02$  %, the material exhibits solid-like behavior (G' > G''), and the Lissajous plot appears as an ellipse, indicating a linear and reversible viscoelastic deformation, although it is non-ideal around (0, 0). As strain increases into the nonlinear regime ( $\gamma = 0.89-3.5 \%$ ), the stress response becomes increasingly distorted, reflecting complex vielding behavior and the progressive transition from solid-like to liquid-like character ( $G''_1 > G'_1$ ). This intermediate region is particularly informative for characterizing the onset and nature of yielding. At  $\gamma$ = 51 %, the material undergoes large-scale, irreversible deformation indicative of structural breakdown and flow, with the stress response dominated by viscous dissipation.

As strain increases beyond the LVR, the shape of the Lissajous curves progressively deviates from an ideal ellipse, reflecting a nonlinear stress response. This distortion signifies that the material stress output is no longer purely sinusoidal and marks the onset of yielding. The inclusion of  $SiO_2$  particles modifies this response. The yield transition region can be quantified by analyzing two key features: the slope of the stress upturn, which relates to intracycle strain stiffening, and the enclosed area of the Lissajous loop, which corresponds to energy dissipated per cycle  $\begin{bmatrix} 32-351 \end{bmatrix}$ .

The strain stiffening factor (S) quantifies the degree of intracycle stiffening and describes how a material's elastic resistance changes with strain in oscillatory shear. A positive S indicates increased stiffness at large strains (strain stiffening), while a negative S indicates reduced stiffness (strain softening). It is calculated from the large-strain modulus ( $G'_L$ ) and the minimum-strain modulus ( $G'_M$ ), as shown in Fig. 6a, and is defined by the following equation:

$$S = \frac{G_L - G_M}{G_L} \tag{1}$$

Strain stiffening behavior was evident beyond the LVR, as indicated by the upward curvature in the stress response of the Lissajous curves at strain amplitudes of 0.89 % and 3.5 %. The corresponding calculated values of the strain stiffening factor at these strain levels are presented in Fig. 6b and c, respectively.

At a strain amplitude of 0.89 % (Fig. 6b), the Mg(OH)2-only suspension exhibited a strain stiffening factor of ~0.75, indicating moderate intracycle stiffening. The addition of 100 nm SiO2 particles had minimal influence on S at this strain level, suggesting only a weak effect on the initial stages of yielding. However, the introduction of larger SiO<sub>2</sub> particles (250, 500, and 800 nm) produced notable, concentrationdependent variations in strain stiffening. At a 29:1 vol%:vol% Mg (OH)<sub>2</sub>:SiO<sub>2</sub> ratio, all three sizes led to increased S values, reflecting enhanced elastic response under deformation, although the behavior is not yet fully understood. At higher SiO2 concentrations (28:2 and 27:3 vol%:vol%), the effect became more differentiated: 250 nm particles induced a slight decrease in S ( $\sim$ 0.725), while 500 nm particles caused the most pronounced reduction, lowering S to 0.70 and 0.65, respectively. In contrast, 800 nm particles generally showed no reduction in S across all tested concentrations. The mechanism for this remains unclear but may be related to particle jamming as the sizes of the two particle types approach equivalence. However, these observations suggest that 500 nm SiO<sub>2</sub> is particularly effective at suppressing strain stiffening and disrupting the particulate network, indicative of a more compliant, less resistant network structure. This behavior aligns with the creep data (Fig. 3), where the presence of 500 nm SiO<sub>2</sub> induced a more gradual yielding process, seen in the delay in increasing creep compliance followed by multiple transitions of creep displacement over time. By reducing intracycle stiffening, it shows the SiO<sub>2</sub> is able to disrupt the Mg(OH)<sub>2</sub> network, modifying the Mg(OH)<sub>2</sub>-Mg(OH)<sub>2</sub> particle contacts in a way that lowers their resistance to mobility.

At 3.5 % strain (Fig. 6c), the influence of particle size was less pronounced. All SiO<sub>2</sub>-containing suspensions showed increased loop asymmetry and exhibited reduced strain stiffening compared to the Mg (OH)<sub>2</sub>-only control, consistent with increased energy dissipation and a more viscous response. As this strain level lies beyond the crossover point of G'<sub>1</sub> and G''<sub>1</sub>, the material is already in a post-yield regime. Therefore, while differences in *S* at this stage reflect variations in viscoelastic character, they offer limited insight into the initial yielding behavior compared to the responses observed at lower strain

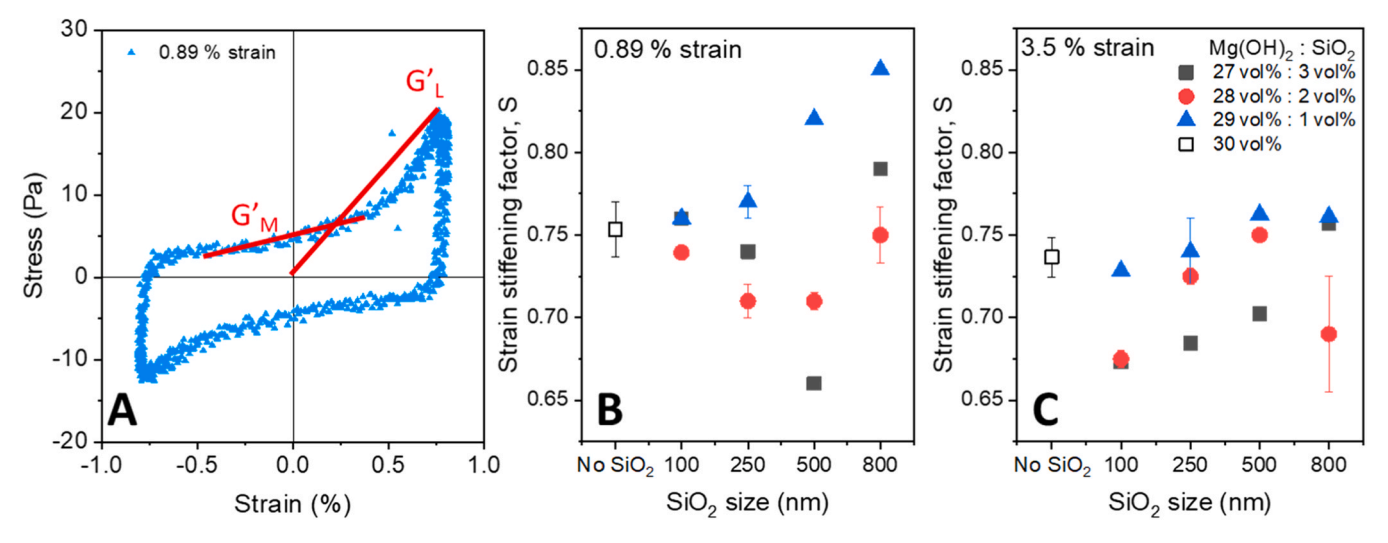


Fig. 6. a) Example Lissajous cycle illustrating the definitions of the slopes used to determine the minimum strain modulus (G'<sub>M</sub>) and large strain modulus (G'<sub>L</sub>) used to calculate the strain stiffening factors (Eq.1). Measured at b) 0.89 % strain and c) 3.5 % strain as a function of Mg(OH)<sub>2</sub>:SiO<sub>2</sub> concentration (vol%:vol%) and SiO<sub>2</sub> particle size (No SiO<sub>2</sub>, 100 nm, 250 nm, 500 nm and 800 nm). Figure legend C also applies to B.

#### amplitudes.

Fig. 7 shows energy dissipation values derived from the Lissajous plots (Fig. 5) at strain amplitudes of 0.89 % and 3.5 %, highlighting the influence of  $SiO_2$  particle size and concentration on dissipative behavior during deformation. Compared with the binary suspensions (except 800 nm  $SiO_2$  at 28:2 vol%:vol%), the Mg(OH)2-only suspension exhibited the highest energy dissipated, indicating stronger interparticle friction in the absence of  $SiO_2$ . In most cases, the addition of 100-500 nm  $SiO_2$  particles significantly reduced energy dissipation, due to the  $SiO_2$  particles disrupting the Mg(OH)2-Mg(OH)2 contacts.

The effect of particle size on reducing energy dissipated during yielding does not appear consistent for all  $\mathrm{SiO}_2$  concentrations. For the lowest  $\mathrm{SiO}_2$  concentration, the reduction in energy dissipated is greatest for  $100~\mathrm{nm}~\mathrm{SiO}_2$  and then decreases with increasing particle size, while for the intermediate concentration the effect appears mostly consistent except for the  $800~\mathrm{nm}~\mathrm{SiO}_2$ , and for the highest  $\mathrm{SiO}_2$  concentration the trend of lowering the dissipated energy increases from  $100~\mathrm{to}~\mathrm{500}~\mathrm{nm}$ , clearly showing the better performance of  $500~\mathrm{nm}~\mathrm{SiO}_2$  to lower energy dissipation during yielding.

The differences in behavior observed at varying volume ratios likely reflect the combined effects of particle dispersion and distribution. For example, with  $100 \text{ nm SiO}_2$ , the energy dissipated shows little variation with increasing volume fraction, suggesting that even at 1 vol% there is already an excess of "active" particles in the suspension, and additional SiO<sub>2</sub> has little effect. This is consistent with the very high particle number ratio calculated for this size, where SiO<sub>2</sub> particles are in significant excess relative to  $Mg(OH)_2$ . A similar trend is observed for the 250 nm particles, likely for the same reason.

In contrast, for the  $500 \text{ nm SiO}_2$  particles a clear reduction in dissipated energy is seen as concentration increases (Fig. 7, 0.89 % strain), indicating that adding more  $SiO_2$  is beneficial. At this size, the number ratio shows that  $SiO_2$  is not in great excess compared to  $Mg(OH)_2$ , so additional particles enhance the effect. A comparable trend is also observed for 800 nm particles, where increasing  $SiO_2$  content generally reduces energy dissipation, although the 2 vol% case appears as a slight outlier without a clear explanation. Overall, for both 500 and 800 nm particles, higher concentrations are favorable for rheology modification.

These results suggest that rheology modification depends on the

number of "active" particles, those capable of modifying contacts between Mg(OH)<sub>2</sub> particles. Based on the number ratios in Table 1, one might expect 100 nm SiO<sub>2</sub> to produce the greatest modification. However, this is not the case, likely due to the large SiO<sub>2</sub> clusters that prevent many particles from contributing. For instance, a single cluster of volume  $1\times10^5~\mu\text{m}^3$  (the lower detection threshold in XRT imaging) contains  $\sim\!1.4\times10^8$  individual 100 nm SiO<sub>2</sub> particles, effectively rendering a large fraction of SiO<sub>2</sub> inactive for yield stress reduction. This highlights the importance of particle dispersion, i.e., breaking down clusters, to maximize the contribution of individual particles/ smaller aggregates.

As previously discussed, the 500 nm  ${\rm SiO_2}$  particles form the fewest clusters, indicating good dispersion, and when added at 3 vol%, produces the most pronounced modification of suspension rheology. Although the 800 nm particles are similarly well dispersed, their number ratio is less favorable than that of the 500 nm particles. These findings therefore highlight the importance of optimizing both particle dispersion and distribution and, together with the imaging data, point to an additional rheology-modifying mechanism, which we propose to be akin to a ball-bearing action.

#### 4. Conclusions

This study examined the reduction of yield stress in concentrated Mg (OH) $_2$  suspensions by adding SiO $_2$  nanoparticles of varying sizes and concentrations. The effect on yield stress was evaluated using creep and large amplitude oscillatory shear (LAOS) rheology. At a Mg(OH) $_2$ -to-SiO $_2$  volume ratio of 28:2, binary suspensions containing 100, 250, 500, and 800 nm SiO $_2$  all exhibited lower yield stresses than the 28 vol% Mg (OH) $_2$ -only suspension, with the greatest reduction observed for 500 nm SiO $_2$ .

Creep measurements revealed a softer yielding transition in the presence of  $\mathrm{SiO}_2$ , with the extent of softening dependent on particle size. Multi-step creep was observed in  $\mathrm{SiO}_2$ -containing suspensions, in contrast to the more abrupt and brittle yielding seen in Mg(OH) $_2$ -only systems. LAOS experiments showed that the largest decrease in strain stiffening and intracycle energy dissipation also occurred with 500 nm  $\mathrm{SiO}_2$ , confirming this size as optimal for modifying the Mg(OH) $_2$  network's yield stress.

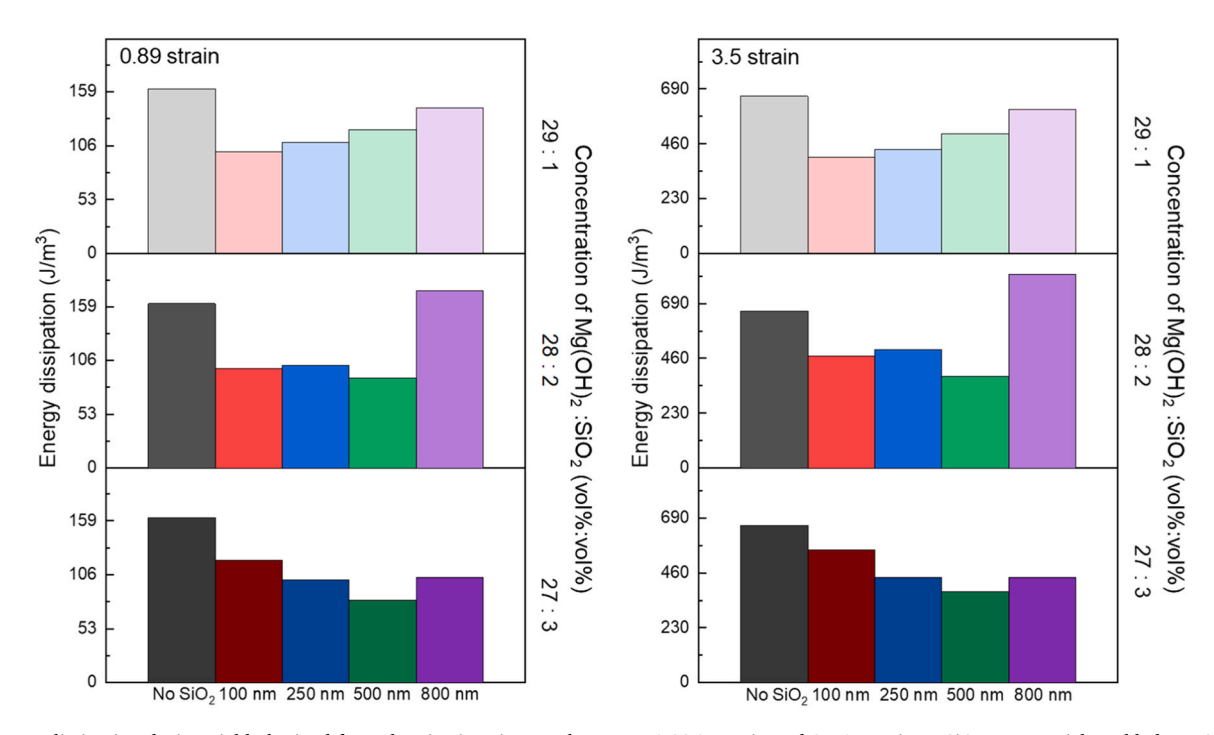


Fig. 7. Energy dissipation during yield obtained from the Lissajous intracycle area at 0.89 % strain and 3.5 % strain vs SiO<sub>2</sub> nanoparticles added. No SiO<sub>2</sub> (grey), 100 nm (red), 250 nm (blue), 500 nm (green) and 800 nm (purple), measured for all concentrations (29:1, 28:2 and 27:3 vol% Mg(OH)<sub>2</sub>:SiO<sub>2</sub>).

SEM and X-ray computed tomography imaging indicated good dispersion of the 500 nm  ${\rm SiO_2}$  compared with smaller  ${\rm SiO_2}$  particles, which were more strongly aggregated. Although 800 nm  ${\rm SiO_2}$  dispersed equally well, its impact on rheology was limited by its low particle number density.

Importantly, these results show that yield stress reductions can be achieved even when the additive is not present in sufficient quantity to restructure the sediment's stress network or coat primary particles to alter their electrical double layer effect. This suggests an alternative mechanism, such as the proposed "ball-bearing" lubrication effect, is likely responsible for the observed reductions.

#### CRediT authorship contribution statement

David Harbottle: Writing – review & editing, Supervision, Methodology, Funding acquisition, Conceptualization. Martyn Barnes: Writing – review & editing, Supervision, Investigation, Funding acquisition, Conceptualization. Timothy Hunter: Writing – review & editing, Supervision, Investigation, Funding acquisition. Vyacheslav Kachkanov: Data curation. Alexander Lockwood: Writing – review & editing, Supervision, Methodology, Funding acquisition, Data curation. Olivia Pickup: Writing – review & editing, Writing – original draft, Methodology, Formal analysis, Data curation. Leonard Turpin: Data curation.

## **Declaration of Competing Interest**

The authors declare that they have no known competing financial interests or personal relationships that could have appeared to influence the work reported in this paper.

## Acknowledgements

This research was supported by funding from the Engineering and Physical Sciences Research Council (EPSRC) through the Centre for Doctoral Training in Nuclear Energy – GREEN (Growing skills for Reliable Economic Energy from Nuclear) (EP/S022295/1). The authors gratefully acknowledge Sellafield Ltd. for providing project funding, and appreciate their valuable expertise and input to guide the project. We also wish to acknowledge the allocation of synchrotron X-ray beamtime at the Diamond-Manchester Imaging beamline (I13–2), provided by Diamond Light Source, UK.

# Appendix A. Supporting information

Supplementary data associated with this article can be found in the online version at doi:10.1016/j.colsurfa.2025.138302.

# Data availability

Data DOI: https://doi.org/10.5518/1752.

### References

- M. Moan, T. Aubry, F. Bossard, Nonlinear behavior of very concentrated suspensions of plate-like kaolin particles in shear flow, J. Rheol. 47 (6) (2003) 1493–1504
- [2] T. Tadros, Interparticle interactions in concentrated suspensions and their bulk (Rheological) properties, Adv. Colloid Interface Sci. 168 (1) (2011) 263–277.
- [3] J.F. Morris, A review of microstructure in concentrated suspensions and its implications for rheology and bulk flow, Rheol. Acta 48 (8) (2009) 909–923.
- [4] E.M. Tracey, P.A. Smith, E.V. Morrey, Rheology of concentrated, heterogeneous slurries containing > 1M electrolyte — a case study in nuclear waste suspensions, J. Nucl. Mater. 230 (1) (1996) 19–35.
- [5] S. Farrokhpay, G.E. Morris, D. Fornasiero, P. Self, Stabilisation of titania pigment particles with anionic polymeric dispersants, Powder Technol. 202 (1) (2010) 143–150.

- [6] H.S. Joyner, Nonlinear (Large-Amplitude Oscillatory Shear) Rheological Properties and Their Impact on Food Processing and Quality, 12(Volume 12, 2021) (2021) 591-609.
- [7] X. Wang, L. Guo, Effect of ionic strength on rheological properties of binary Al2O3/ ZrO2 suspensions, Colloids Surf. A Physicochem. Eng. Asp. 297 (1) (2007) 7–13.
- [8] J.L. Dávila, M.A. d'Ávila, Laponite as a rheology modifier of alginate solutions: physical gelation and aging evolution, Carbohydr. Polym. 157 (2017) 1–8.
- [9] A. Potanin, Rheology of silica dispersions stabilized by polymers, Colloids Surf. A Physicochem. Eng. Asp. 562 (2019) 54–60.
- [10] S. Kim, K. Hyun, J.Y. Moon, C. Clasen, K.H. Ahn, Depletion stabilization in nanoparticle–polymer suspensions: multi-length-scale analysis of microstructure, Langmuir 31 (6) (2015) 1892–1900.
- [11] O. Pickup, L. Turpin, V. Kachkanov, R. Mitchell, M. Barnes, A. Lockwood, T. N. Hunter, D. Harbottle, Yield stress modification of suspensions of irregularly shaped particles by addition of spherical colloidal silica, Colloids Surf. A Physicochem. Eng. Asp. 693 (2024) 134062.
- [12] N. Madhavan, A.P. Deshpande, E. Mani, M.G. Basavaraj, Electrostatic heteroaggregation: fundamentals and applications in interfacial engineering, Langmuir 39 (6) (2023) 2112–2134.
- [13] P. Bansal, A.P. Deshpande, M.G. Basavaraj, Hetero-aggregation of oppositely charged nanoparticles, J. Colloid Interface Sci. 492 (2017) 92–100.
- [14] P.D. Yates, G.V. Franks, S. Biggs, G.J. Jameson, Heteroaggregation with nanoparticles: effect of particle size ratio on optimum particle dose, Colloids Surf. A Physicochem. Eng. Asp. 255 (1) (2005) 85–90.
- [15] M. Cerbelaud, M. Muñoz, F. Rossignol, A. Videcoq, Self-organization of large alumina platelets and silica nanoparticles by heteroaggregation and sedimentation: toward an alternative shaping of Nacre-Like ceramic composites, Langmuir 36 (13) (2020) 3315–3322.
- [16] D. Kleshchanok, V. Meester, C.E. Pompe, J. Hilhorst, H.N.W. Lekkerkerker, Effects of added silica nanoparticles on hectorite gels, J. Phys. Chem. B 116 (31) (2012) 9532–9539.
- [17] J. Landman, E. Paineau, P. Davidson, I. Bihannic, L.J. Michot, A.-M. Philippe, A. V. Petukhov, H.N.W. Lekkerkerker, Effects of added silica nanoparticles on the nematic liquid crystal phase formation in beidellite suspensions, J. Phys. Chem. B 118 (18) (2014) 4913–4919.
- [18] L. Bailey, H.N.W. Lekkerkerker, G.C. Maitland, Rheology modification of montmorillonite dispersions by colloidal silica, Rheol. Acta 53 (5) (2014) 373–384.
- [19] L. Bailey, H.N.W. Lekkerkerker, G.C. Maitland, Smectite clay inorganic nanoparticle mixed suspensions: phase behaviour and rheology, Soft Matter 11 (2) (2015) 222–236.
- [20] D. Kong, H. Yang, Y. Yang, S. Wei, J. Wang, B. Cheng, Dispersion behavior and stabilization mechanism of alumina powders in silica sol, Mater. Lett. 58 (27) (2004) 3503–3508.
- [21] A. Singh, C. Ness, A.K. Sharma, J.J. de Pablo, H.M. Jaeger, Rheology of bidisperse non-Brownian suspensions. arXiv. 2023.
- [22] S. Chaki, B. Román-Manso, L. Senatus, J.A. Lewis, K.S. Schweizer, Theoretical study of the impact of dilute nanoparticle additives on the shear elasticity of dense colloidal suspensions, Soft Matter 21 (9) (2025) 1731–1747.
- [23] T. Athar, Chapter 17 smart precursors for smart nanoparticles, in: W. Ahmed, M. J. Jackson (Eds.), Emerging Nanotechnologies for Manufacturing (Second Edition), William Andrew Publishing, Boston, 2015, pp. 444–538.
- [24] N. Wadeson, M. Basham, Savu: A Python-based, MPI Framework for Simultaneous Processing of Multiple, N-dimensional, Large Tomography Datasets.
- [25] Q.D. Nguyen, D.V. Boger, Measuring the flow properties of yield stress fluids, Annu. Rev. Fluid Mech. 24 (1) (1992) 47–88.
- [26] Y. He, A. Hassanpour, A.E. Bayly, Combined effect of particle size and surface cohesiveness on powder spreadability for additive manufacturing, Powder Technol. 392 (2021) 191–203.
- [27] M. Cerbelaud, A. Videcoq, F. Rossignol, M.A. Piechowiak, D. Bochicchio, R. Ferrando, Heteroaggregation of ceramic colloids in suspensions, Adv. Phys. X 2 (1) (2017) 35–53.
- [28] R.B. Rao, V.L. Kobelev, Q. Li, J.A. Lewis, K.S. Schweizer, Nonlinear elasticity and yielding of nanoparticle glasses, Langmuir 22 (6) (2006) 2441–2443.
- [29] T. Voigtmann, Nonlinear glassy rheology, Curr. Opin. Colloid Interface Sci. 19 (6) (2014) 549–560.
- [30] M. Siebenbürger, M. Ballauff, T. Voigtmann, Creep in colloidal glasses, Phys. Rev. Lett. 108 (25) (2012) 255701.
- [31] A. Maestro, O.S. Deshmukh, F. Mugele, D. Langevin, Interfacial assembly of Surfactant-Decorated nanoparticles: on the rheological description of a colloidal 2D glass, Langmuir 31 (23) (2015) 6289–6297.
- [32] K. van der Vaart, F. Depypere, V.D. Graef, P. Schall, A. Fall, D. Bonn, K. Dewettinck, Dark chocolate's compositional effects revealed by oscillatory rheology, Eur. Food Res Technol. 236 (6) (2013) 931–942.
- [33] J. John, D. Ray, V.K. Aswal, A.P. Deshpande, S. Varughese, Dissipation and strainstiffening behavior of pectin–Ca gels under LAOS, Soft Matter 15 (34) (2019) 6852–6866.
- [34] R.H. Ewoldt, A.E. Hosoi, G.H. McKinley, New measures for characterizing nonlinear viscoelasticity in large amplitude oscillatory shear, J. Rheol. 52 (6) (2008) 1427–1458.
- [35] J. Läuger, H. Stettin, Differences between stress and strain control in the non-linear behavior of complex fluids, Rheol. Acta 49 (9) (2010) 909–930.